



Experimental Study of Compact Sandstone Deformation Under Axisymmetric Triaxial Loading Along Specific Paths in Stress Space

Ivan Janeček¹ · Deepak Amban Mishra^{1,2} · Chitralkha Satheesan Vishnu^{1,3} · Jiří Ščučka¹ · Lenka Vaculíková¹ · Petr Martinec¹

Received: 4 January 2023 / Accepted: 18 September 2023 / Published online: 20 October 2023
© The Author(s) 2023

Abstract

The deformation of rocks well below their ultimate strengths is frequently described through the constant stiffness moduli of the linear elasticity theory. In addition, the isotropic material approximation is usually used as the basic approach. Particularly in sedimentary rocks, local inhomogeneities, anisotropy, and irreversible processes, mainly related to the gradual breakage of grain joints, can affect their deformation behavior from the beginning of the loading. Consequently, the stiffness moduli measured under triaxial conditions are effective parameters, which may depend on the loading path in the stress space. Therefore, a complex experimental study of the deformation response of compact sedimentary rock (Brenna sandstone) along various paths in triaxial stress space was prepared to understand this dependence. In addition, a detailed analysis of the rock composition and structure of this compact sandstone was carried out. This paper presents an initial experimental study that is based on a loading method using alternative stress paths that correspond to different modes of the monotonic increase in differential stress from an initial isotropic compression state. In the experiment, the dependence of stiffness moduli on the loading path was found. Differences in rock deformation for conventional triaxial compression and extension can be attributed to a slight rock anisotropy originating from the stratification. The different behavior of deformation and related stiffness moduli along so-called reduced triaxial paths and conventional paths indicates that irreversible processes must be taken into account.

Highlights

- The study brings new experimental data on the deformation of compact sedimentary rock in specific triaxial stress conditions.
- The measured effective stiffness moduli of compact sandstone depends on the loading path in the triaxial stress state.
- In general, the deformation response of the sandstone is nonlinear from the start of loading.
- The mechanical properties of the sandstone show anisotropy as a consequence of stratification.
- In standard triaxial tests, failure criterion combining stress and strain conditions can be used for the investigated sandstone.

Keywords Rock mechanics · Triaxial stress state · Young's modulus · Poisson's ratio · Rock isotropy · Sedimentary rocks · Sandstone

✉ Ivan Janeček
janecek@ugn.cas.cz

¹ Institute of Geonics of the Czech Academy of Sciences, Studentská 1768, 708 00 Ostrava, Czech Republic

² Present Address: Department of Petroleum Engineering & Earth Sciences, Indian Institute of Petroleum and Energy, AUCE Road, 530003 Visakhapatnam, Andhra Pradesh, India

³ Present Address: Borehole Geophysics Research Laboratory, Ministry of Earth Sciences, 415105 Karad, Maharashtra, India

1 Introduction

An experimental investigation of the stress–strain characteristics in various loading regimes is necessary for a comprehensive understanding of the mechanical behavior of the rocks or building materials that are used in underground construction. For theoretical modeling of the deformational response of these materials under general stress conditions, the characteristics used as model inputs should cover a sufficiently representative set of

triaxial stress states. The standard models that are used in many rock mechanics theories and calculations of practical geomechanical tasks are based on mathematical concepts of the linear elasticity theory (Fjar et al. 2008), most of which have adopted the approximation of isotropic rock. This description is mainly justified for stresses that are sufficiently below the ultimate peak strength and is typically extended by some form of plasticity theory, which is used to describe irreversible processes of fracturing in rocks. Under these simplified assumptions, the mechanical quasi-elastic parameters of rock can only be determined by a simple uniaxial compression test. Therefore, the uniaxial compression test is typically used for the rapid testing of these materials. However, from the geomechanics point of view, these commonly used uniaxial conditions are not sufficient, because most underground materials are subjected to a triaxial state of stress, for which the three principal stresses $\sigma_1 \geq \sigma_2 \geq \sigma_3$ can vary independently. In laboratory experiments, this can only be attained through special measuring devices that are traditionally known as true triaxial apparatus, whose construction is more complex (Kwaśniewski 2012; Feng et al. 2019).

The standard triaxial tests (Ulusay et al. 1974) are predominantly carried out in triaxial cells. The standard triaxial tests are typically used to determine the failure envelope, which is necessary to describe the mechanical behavior of rock through plasticity theory. This triaxial test commonly uses the known scheme (Franklin 1983). Initially, the isotropic pressure (equivalent to the horizontal stress σ_h) is increased to a given value. Subsequently, the vertical stress σ_v is continuously increased, while the horizontal stress stays unchanged. One of the alternative names for this test is the conventional triaxial compression or CTC test (Kwaśniewski 2012). A lot of stress–strain data that comes from this most common form of triaxial test can be found in the literature. However, under in situ conditions, the path over stress space can be totally different from the commonly experimented CTC model. For example, some deformation processes during underground excavations and effects such as rock burst or core disking have been attributed to the existence of high initial horizontal stresses in rock massifs. Therefore, laboratory stress conditions that correspond to an axial extension may be closer to reality for these in situ situations, as mentioned in Takemura et al. (2012).

1.1 Alternative Loading Paths in Triaxial Stress State

Many non-standard theoretical paths can be considered to understand the deformational response of rock materials under triaxial stress conditions. However, implementing overly complicated paths can be technically difficult. Therefore, simplified paths consisting of linear segments in 3D stress space are preferred. Several selected specific paths have been used in triaxial cells (Kwaśniewski 2012). These paths typically consist of two parts. In both parts, a linear time evolution of stress (or strain) is preferred for loading or unloading. The first part is isotropic compression (IC), or rarely anisotropic compression (AC) in the form of proportional loading (conservation of ratio of the vertical and horizontal stresses) to predetermined stress values. In the second part, one of the stresses σ_v or σ_h is gradually increased (conventional loading tests) or decreased (unloading tests using reduced stress) to a final value, while the other stress remains constant. Cylindrical samples whose rotational symmetry axis is oriented vertically are typically used in triaxial cells. Depending on these four stress conditions, these samples can undergo compression ($\sigma_v > \sigma_h$) or extension ($\sigma_v < \sigma_h$) along this rotational axis. Therefore, triaxial tests that correspond to these four different situations are usually called: conventional triaxial compression (CTC; which was already mentioned as the standard triaxial test), conventional triaxial extension (CTE), reduced triaxial compression (RTC), and reduced triaxial extension (RTE) (Kwaśniewski 2012).¹ If a true triaxial apparatus is used, then the ensemble of these experimental stress paths can be substantially extended (Feng et al. 2019).

Early studies von Kármán (1911), Böker (1914, 1915) and Murrell (1963) were mainly focused on the evaluation of the importance of the intermediate principal stress for rock failure. The influence of triaxial extension conditions on the permeability and porosity of porous sandstones was investigated by Zhu et al. (1997). Other experiments have used the confining extension path to investigate the relation between fracture angle and confining pressure in homogeneous and isotropic Carrara marble (Ramsey and Chester 2004). Experiments with indirect triaxial extension have been followed by new studies that use direct axial extension (more technically feasible) in triaxial conditions (Liu et al. 2021; Zeng et al. 2019; Cen and Huang 2017). In addition to the study of deformation, the triaxial extension paths were also used to analyze the changes in porosity and permeability in the axial direction that were caused by radial stress (Zhu et al. 1997).

¹ See Sect. 3 for technical details.

The specific loading stress paths (usually consisting of initial isotropic compression and additional sequential uniaxial or biaxial loading and unloading) generated by triaxial apparatus were used to investigate the inelastic processes in rocks (Panteleev et al. 2020a, b), particularly the Kaiser effect during loading /unloading in different principal directions. Using a true triaxial device, Ingraham et al. (2012, 2013a, b) studied the evolution of damage and localization of deformation (formations of shear bands and localized compaction) in sandstones along different stress paths (in octahedral stress planes) corresponding to several values of the Lode angle invariant and mean stress. The important role of the intermediate principal stress in rock failure was confirmed. Another experiment that compared the deformation behavior of sandstones of different porosities under true triaxial conditions was performed by Ma and Haimson (2016), who found that the effect of intermediate principal stress on rock failure was higher for sandstone with lower porosity.

Recently, a few authors Takahashi et al. (2012), Takemura et al. (2012) and Panaghi et al. (2021) have focused on the precise measurement of strains (or even a deeper analysis of the behavior of stiffness moduli) under the triaxial loading along the non-standard paths.

1.2 Motivation for This Study

In published papers on multiaxial testing, strength data from the alternative stress paths were mainly presented and discussed. However, the corresponding deformation data in the so-called elastic region (if published at all) were not analyzed in detail, and the corresponding stiffness moduli from these alternative paths were rarely compared (Panaghi et al. 2021).

The natural consequence of the linear theoretical approaches is that the deformational response of rock along any other loading paths in the stress state can be calculated through the superposition principle. This should be valid for reversible deformation, at least. However, the superposition validity could potentially even be extended for total deformation if only pure loading paths² are considered.

For these reasons, some basic questions that relate to the real deformational response of rock are to be addressed. Can the reversible or even pure loading strains be superposed to obtain the deformational response to a general stress state, which is far enough from the rock failure surface (corresponding to the ultimate strength)? What role does the structural anisotropy of rocks play, especially in sedimentary rocks with a layered structure that often shows local irregularities? The answers to these questions are not clear or easy. Hence, a detailed experimental investigation of the

real deformational response of rocks along non-standard paths is very desirable.

2 Material Characteristics

For our study, a medium-grained sandstone from a surface quarry near the Brenna in Beskid Slaski Mountains (Beskid of the Silesian region) in the south of Poland was selected. The sandstone of Cretaceous age originates from the Middle Member of the Godula Formation of the Outer Western Carpathians flysch (Silesian unit). The thickness of the sandstone layers is around 2.5 m, and is slightly cut by claystones and mudstones. Visually, this compact sandstone typically exhibits good homogeneity of the sample material (without apparent cracks) on a macroscopic scale. The uniaxial strength is relatively high, ranging from 100 to 130 MPa, as reported by Kwaśniewski and Takahashi (2010). During loading, this sedimentary material shows significant and reproducible changes in volume, which include the transition from the contractant to the dilatant mode of volumetric deformation. These facts confirm that Brenna sandstone is a suitable candidate for our planned experimental studies. Before starting our mechanical experiments, the petrographic, physical, and chemical analyses were carried out to characterize the structure and composition of the investigated rock.

2.1 Brenna Sandstone Composition

The composition of the sandstone and the determined sizes of its framework grains are shown in Table 1. The framework of this sedimentary siliciclastic rock is formed by close contact of larger grains originating from primary sediment clasts.³ These framework grains are strongly bonded through crystal inter-growth or by cement, which was formed as a secondary material by the chemical precipitation of primary minerals during diagenesis. The framework includes the stable component that dominates and a non-stable component.

The stable component consists mainly of quartz grains and quartzite fragments, while the chert content is substantially less. In addition, other stable rock fragments (mainly quartz-feldspar grains) are present. The quartz grains are angular to sub-angular in shape, with a medium degree of sphericity, and demonstrate the presence of authigenic quartz. The quartzite grains are sub-angular, and with observed surface corrosion. The chert grains and fragments of stable rocks vary greatly in shape and size.

The non-stable component includes feldspar grains, mica flakes (mostly muscovite), and fragments of non-stable

² i.e., involving only increasing uniaxial, biaxial, or triaxial compressions.

³ According to the definition of sandstone framework, this includes grains of sizes from 0.0625 to 2 mm (i.e., sand grain size).

Table 1 Brenna sandstone composition average and maximum grain sizes (*a* and *b* represent the maximum and minimum linear dimensions of individual grains, respectively)

	Content %vol.	Grain size (comments)				Sphericity (shape)
		Avg. <i>a</i> (mm)	Avg. <i>b</i> (mm)	Max. <i>a</i> (mm)	Max. <i>b</i> (mm)	
Framework	88					
<i>Tot. stable</i>	<i>79</i>					
Quartz	49	0.15	0.08	0.80	0.40	0.4–0.8
Quartzite	18	0.20	0.10	1.10	0.40	0.2–0.6
Chert	4	0.05	0.05	0.20	0.10	0.4–0.6
Other rock frag.	8	0.16	0.09	0.60	0.38	0.4–0.6
<i>Tot. non-stable</i>	<i>9</i>					
Micas	3	0.25	0.03	0.50	0.05	(<i>flakes</i>)
Feldspar	2	0.20	0.17	0.30	0.26	0.4–0.6
Rock frag.	4	0.20	0.20	1.50	0.60	0.2–0.6
Matrix	12					
Phyllosilicates	5	(Fine particles—“clay”)				
Quartz	4	(Fine particles and cement)				
Carbonate	2	(Cement and calcite monocrystals)				
Glauconite	1	0.10	0.08	0.20	0.18	(<i>Pellets</i>)

The sums of the contents of the framework and matrix components are highlighted in bold, i.e., 88% + 12% = 100%

Row group headings for stable and unstable components are italicized. To the right of these headings, the summary contents of these components are shown in italics, i.e. 79% + 9% = 88% (frame content)

rocks. The feldspars are represented by K-feldspars (orthoclase and microcline) and Na–Ca-feldspars (plagioclase series from oligoclase to andesine). Feldspar grains are argillitised to varying degrees. Their sizes are variable, but are usually close to the sizes of quartz grains. The identified muscovite flakes show surface illitization and syndimentary deformation, which is also evident on non-stable rock fragments. The observed non-stable rocks are sedimentary rocks (siltstones, greywackes, or carbonates), granitoids, and gneisses.

On the microscopic scale, the rock material exhibits an anisotropy due to the deposition of elongated grains (including the mica flakes) sub-parallel to the bedding planes. Framework grains are surrounded by matrix (or ground mass).⁴

The matrix mainly consists of fine particles of primary quartz and phyllosilicates (illite, kaolinite), which are typically bound through (secondary) quartz- and carbonate-cement. In addition, newly formed rims were found on primary quartz framework grains. The carbonate cement also occurs in the form of larger calcite single crystals, but their volumetric fraction is negligible. An authigenic glauconite was present in the form of isolated pellets in inter-granular

pores. The volumetric fraction of this glauconite is also negligible.⁵ Some of the important rock components can be identified in the micro-photographs of this rock, which are shown in Fig. 1.

The porosity of Brenna sandstones depends on the degree of sorting in the rock. Values of the porosity have been calculated from bulk density (i.e., effective volumetric mass density) and particle density of the solid phase (i.e., average intrinsic volumetric mass density). The bulk density of dry Brenna sandstone varies from 2380 to 2470 kg/m³ in the material used for our experiment, while the typical particle density of the solid phase (determined through He-densitometry) is from 2629 to 2648 kg/m³. The calculated porosities range from 6 to 8 %. The structure of the rock pores is mostly of the configurational-cementitious type (primary pore space is formed by mutual configuration of clastic grains and the secondary space is filled with the cemented matrix). Microscopic analysis, together with Hg-porosimetry results, indicates that the pore system of the rock also contains inter-granular slit-like pores, tracing the surface of clastic grains. These pores can frequently coalesce and constitute natural fracture interfaces that approximately follow the direction of bedding (Fig. 2). The existence of these interfaces can be attributed to the layer structure of the

⁴ The presented volume fraction of matrix includes all fine particles (sizes less than 0.0625 mm) in the sedimentary rock, together with any secondary mineral matter arisen during diagenesis (cement or other authigenic particles).

⁵ The specific green color of glauconite is responsible for the typical gray-green or blue-green color of the investigated sandstone.

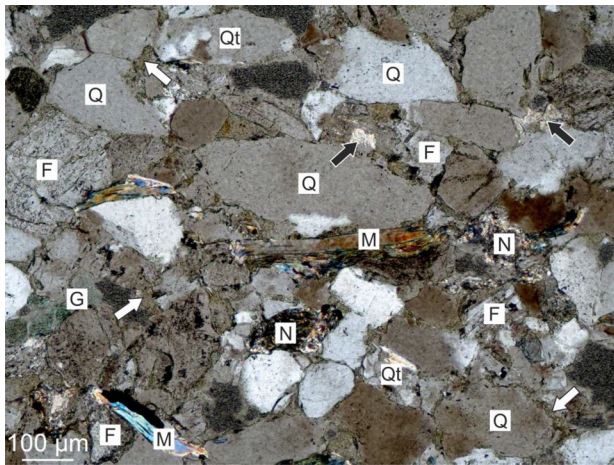


Fig. 1 Micro-photograph of the mineral composition and rock fabric anisotropy of the Brenna sandstone. The rock consists of elongated clastic grains and mica flakes oriented sub-parallel to bedding planes (*Q* quartz, *Qt* quartzite, *F* feldspars, *G* glauconite, *M* micas, *N* non-stable rock fragments, white arrow—matrix, black arrow—carbonate cement in configuration pores)

sedimentary rock. The presence of thin laminae of deposited clay matter is typical for this otherwise very compact material. The formation of these inhomogeneities is accompanied by diagenetic cementation of the pores and matrix, while weathering or biogenic mineralization do not play a role.

2.2 Rock Samples

A set of cylindrical samples (with diameters of 50 mm and heights of 100 mm and with the rotational axis approximately perpendicular to the plane of stratification; see Fig. 3) was prepared from rock material. The rotational-symmetry axis of the cylindrical samples corresponds to the original vertical direction in situ (i.e., it is perpendicular to the plane of stratification).

3 Experimental Technique and Methods

3.1 Monotonic Triaxial Loading

Four sets of triaxial tests corresponding to the four alternative loading paths (CTC, RTE, CTE, and RTC) were performed to compare the deformation response of this rock in a hypothetical quasi-elastic stress region. In addition, complete CTC curves were determined to analyze the rock failure conditions. For the cylindrical rock samples that were used for the measurements in the triaxial chamber, the vertical axis of the laboratory coordinate system coincides with the rotational-symmetry axis of the cylinder. Therefore,

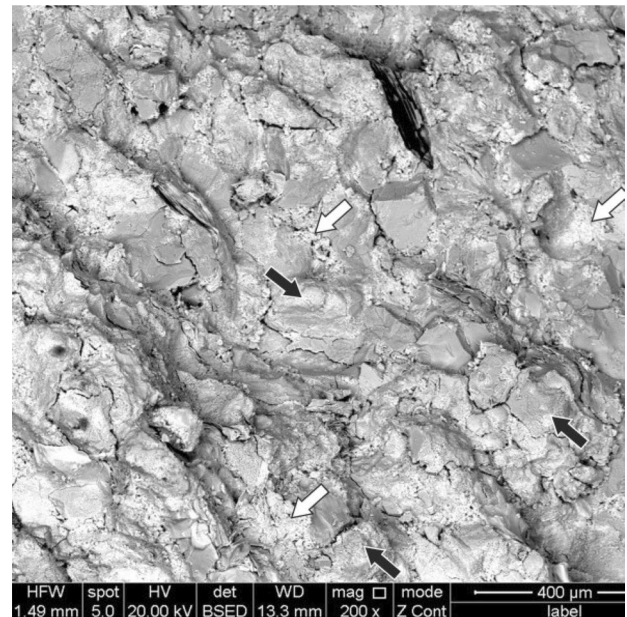


Fig. 2 SEM micrograph of a natural fracture surface in the Brenna sandstone. The fracture surface is parallel to the bedding planes (white arrow—configuration pores filled with carbonate cement; black arrow—thin coating of the matrix on the surface of clastic grains. The surface corresponds to the original coalesced slit-like pores. Moreover, some isolated slit-like pores that are oriented transversely to the surface are visible)



Fig. 3 A sample of the Brenna sandstone prepared for mechanical testing

the terms axial compression and axial extension are used throughout this paper to emphasize the direction of the

sample deformation. In the standard CTC triaxial test, σ_v increases, which causes additional axial compression (following the isotropic compression). Meanwhile, in RTE the σ_v is reduced and the sample is axially extended. CTE uses increasing σ_h to achieve axial extension; while in RTC σ_h is reduced and thereby causes axial compression. In terms of modeled principal stresses, the intermediate principal stress is minimum ($\sigma_2 = \sigma_3$) for axial compression (CTC and RTC) and maximum ($\sigma_2 = \sigma_1$) for axial extension (CTE and RTE).

For measurements of stress–strain characteristics, a new, sophisticated, and universal experimental device for rock mechanics (a servo-controlled hydraulic system with a triaxial chamber produced by MTS System Corporation) was utilized. The basic properties and technical parameters of this device (including a description of the measurement-detectors) are summarized in Appendix 1.

The horizontal stress $\sigma_h = p$, and the vertical stress can be expressed as $\sigma_v = \sigma_d + p$, where the stress difference σ_d ⁶ is positive for axial compression, negative for axial extension, and zero for isotropic compression. The variables σ_d , p represent two independent control channels in our system and can be used as alternative to the original stress components σ_v and σ_h . In Fig. 4, these two variants of variables are used for graphical representation of the paths discussed above (i.e., IC, AC, CTC, RTC, CTE, and RTE). All of the above-mentioned tests were performed at various initial isotropic pressures $p^{(i)}$, ranging from 10 to 120 MPa at an interval of 10 MPa.

The axial load limited by the maximum range (2.6 MN) of the in-chamber load cell allows the complete stress–strain curve along a CTC stress path to be determined up to the failure of rock at all initial isotropic pressures that are attainable in the used type of triaxial chamber (up to 140 MPa). In these initial CTC tests, the additional axial loading was controlled by axial strain. This strain control mode is technically feasible and well tunable because the in-chamber horizontal stress $\sigma_h = p$ is kept constant (at the value of initial isotropic pressure) through the stress control mode. The time evolution of the stress difference σ_d can be controlled by feedback, either directly via the voltage signal of the internal load cell or indirectly via the signal from the axial extensometer. Axial displacement measured directly on the sample was changed at a constant rate of about 0.001 mm/s. The corresponding axial stress rates in the CTC tests varied in range from about 0.2–0.7 MPa/s. For the other three tests (i.e., RTC, CTE, and even RTE), the strain control is technically problematic. However, the technical upper limits for differential stress σ_D that is valid in these three tests was sufficiently far from the failure point of investigated sandstone, especially for higher applied confining pressures

p . Therefore, for these three groups of tests, as well as for initial isotropic compression, the control by stress is fully sufficient. For the stress-controlled tests (i.e., for loading and unloading of vertical or horizontal stress), the universal constant stress rate $\dot{\sigma} = 0.25$ MPa/s was used. Corresponding axial displacement rates ranged from about 0.0002–0.0015 mm/s.

3.2 Determination of Stiffness Moduli

Despite the fact that the measured stress–strain characteristics of rocks are generally non-linear, the constant stiffness moduli based on the linear elastic media approach are commonly used to describe the deformation behavior of rocks below the failure limit. This idealization is often accepted in practice for geotechnical estimates, or even for numerical simulations of rock masses.⁷ In addition, the simplest model uses assumptions about the approximate homogeneity of the material at the given scale and isotropy. Sufficient homogeneity is mainly a matter of choosing a representative sample of the material. The anisotropy of rocks can often be considered low; it mainly depends on whether the variations due to the anisotropy of the rock are more significant than the variations due to inhomogeneity. On the other hand, it is known that the apparent anisotropy of material can affect, for example, crack tip fields and therefore the fracture behavior of rock (Ayatollahi et al. 2022). In the quasi-elastic region, an anisotropic description is sometimes proposed, which is inspired by the elastic behavior of ideal crystals with exact symmetries. However, a real rock is a conglomerate of very diversely oriented grains. The direction distribution can be quite complicated, and the definition of the axes of symmetry can be questionable. A much more complex model may not always provide better results. Moreover, this description needs many more elastic parameters, so many more measurements should be performed for different sample orientations. An isotropic model needs two independent parameters determined by a single measurement on a single sample. These are the reasons why this model is still used in geotechnics as the roughest approximation. Therefore, for the initial processing and analysis of measured data, a simplified elastic model assuming a homogeneous isotropic sample, which is exposed to the required triaxial stress state conditions, will be considered. Based on the results of this initial

⁶ Here $\sigma_d \equiv \sigma_v - \sigma_h$. The absolute value of σ_d is equivalent to differential stress $\sigma_D \equiv \sigma_1 - \sigma_3$ (being always positive by the definition).

⁷ Two basic concepts are suggested to determine the approximative constant stiffness moduli: (1) mean constant moduli for a selected region of stresses, and (2) secant moduli calculated from two selected representative points on stress–strain characteristic. However, the average constant stiffness moduli that were obtained by linear fit only represent an acceptable approximation for regions where the stress–strain curves are approximately linear. Meanwhile, any conventional secant stiffness moduli represent only very rough compromise estimates.

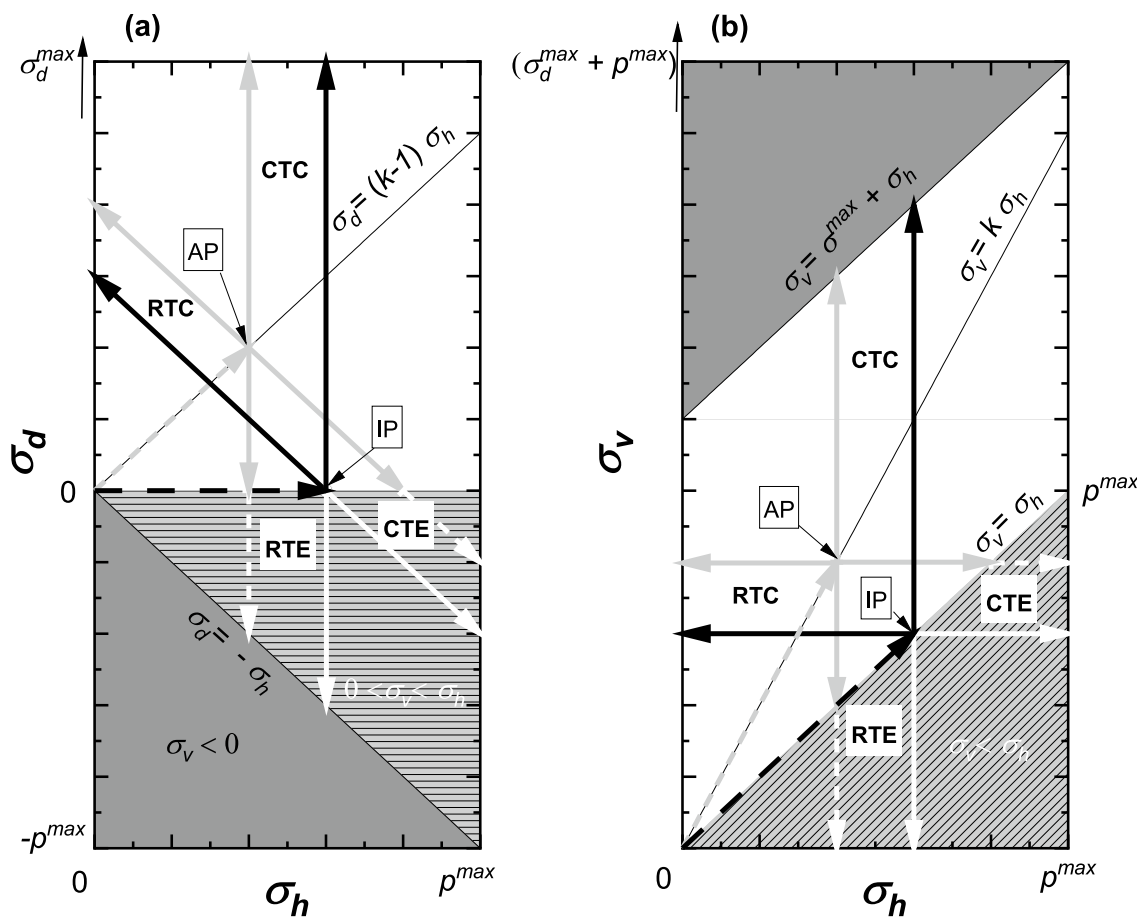


Fig. 4 Loading paths in stress space: **a** $[\sigma_d, p]$, and **b** $[\sigma_v, \sigma_h] = [\sigma_d + p, p]$. Initial loadings: *IC* isotropic compression (dashed line) to isotropic state P_I or *AC* anisotropic compression (dotted line) to anisotropic state P_A (example: $\sigma_1 = 2p$). Final loadings:

CTC conventional triaxial compression, *RTE* reduced triaxial extension, *RTC* reduced triaxial compression, *CTE* conventional triaxial extension

treatment, the role of sandstone anisotropy in the deformation mechanism will be discussed. The formulae to calculate the bulk modulus K , the Young's modulus E , and the Poisson's ratio ν can be obtained through derivatives of the linear deformational responses of the ideal model material subjected to loading modes *IC*, *CTC/RTE* and *CTE/RTC* (see Appendix 2). The formulae for E and ν have different forms for triaxial tests *CTE/RTC* (Eqs. 6, 7) and *CTC/RTE* (Eqs. 4, 5). The stiffness moduli determined through these formulae can be used for a better comparison of the results from both tests. However, in a real experiment, the stiffness moduli may not generally be constant and uniform parameters. Therefore, their behavior under different stress conditions must be carefully analyzed. Linear regions can often be found for axial strain characteristics under axial loading, but a linear deformational response is very rare for lateral strains. In this case, the selection of the region for linear interpolation is often a very subjective choice, which can significantly affect the determined Poisson's ratio values.

The derived formulae (Eqs. 4, 5) can even be accepted for the determination of tangential stiffness moduli at given stress conditions under the assumption of approximate validity of the superposition principle for strains. Clearly, the effective tangential stiffness moduli $E(\sigma_d, p)$ and $\nu(\sigma_d, p)$ defined through the Eqs. (4) and (5) do not need to be constant for nonlinear characteristics.

In this study, an alternative but equivalent calculation of the effective stiffness moduli was used. This calculation is based on the standard Eqs. (4) and (5). However, the *CTC/RTE* stiffness moduli were treated directly from measured axial and lateral strains, while the *CTE/RTC* stiffness moduli were calculated from theoretical *CTC/RTE* (1D) stress-strain characteristics that were obtained through formal decomposition of *CTE/RTC* (2D) experimental strain curves through formulae based on superposition principle and sample isotropy:

Fig. 5 Stress–strain characteristics of complete standard CTC tests. For the test, $\sigma_d = \sigma_D \equiv \sigma_3 - \sigma_1$ and $p^{(i)}$ are initial pressures. Strains: axial strain ϵ_a (full lines) and lateral strain ϵ_c (dashed lines), and volumetric strain ϵ_{Vol} . The opposite sign at σ_d was only used to move the volumetric strain curves to the fourth quadrant to avoid overlapping the curves of individual groups

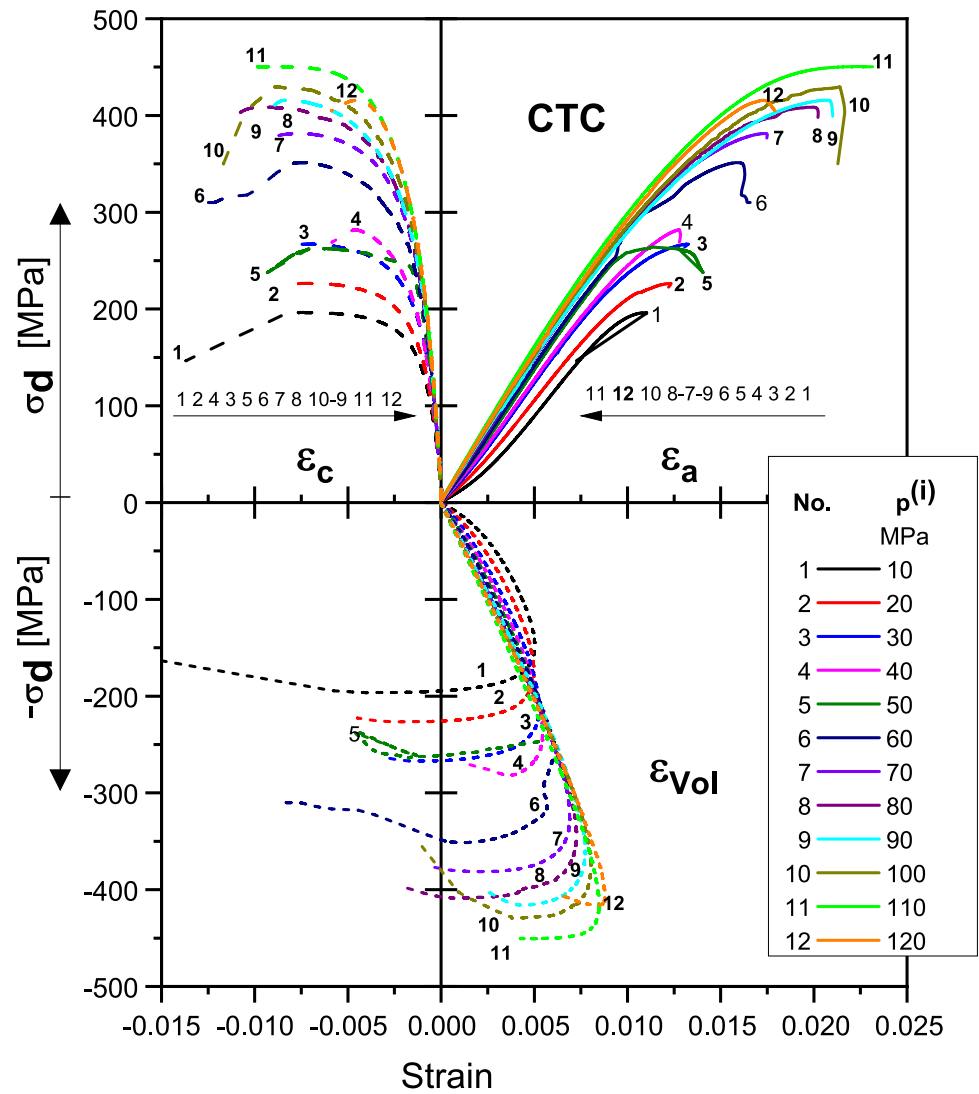


Table 2 Selected parameters from the complete CTC tests (strains ϵ_a and ϵ_v only represent the parts generated by increasing the differential stress σ_D)

Initial pressure p (MPa)	Differential stress thresholds and related strains				
	$\sigma_{D,TD}$ (MPa)	$\epsilon_{v,max}$ (m/m)	$\sigma_{D,max}$ (MPa)	$\epsilon_a(\sigma_{D,max})$ (m/m)	$\epsilon_v(\sigma_{D,max})$ (m/m)
10	148	0.00502	196	0.01099	-0.0039
20	179	0.00496	227	0.01233	-0.0023
30	202	0.00520	267	0.01322	-0.0009
40	240	0.00545	282	0.01276	0.0036
50	240	0.00575	264 ^a	0.01274	-0.0018
60	255	0.00616	351	0.01591	0.0011
70	325	0.00689	381	0.01735	0.0022
80	345	0.00725	409	0.02001	0.0007
90	362	0.00773	416	0.02064	0.0044
100	376	0.00803	430	0.02140	0.0038
110	416	0.00847	451	0.02210	0.0051
120	411	0.00876	416 ^a	0.01729	0.0083

^aValues deviating from the otherwise monotonic increase in the maximum ultimate strength with the confining pressure. These exceptions may be caused by the existence of local defects due to natural variability

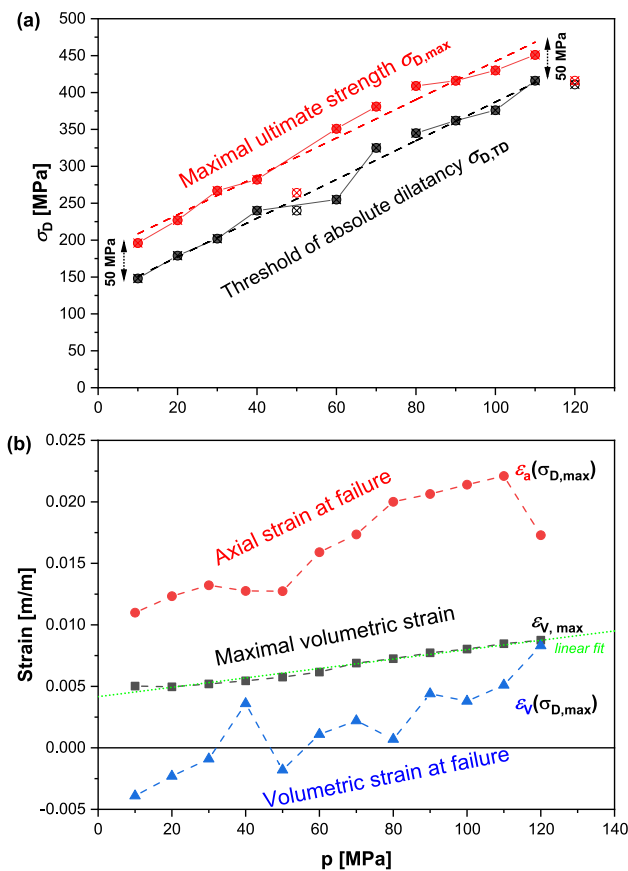


Fig. 6 Dependence of characteristic stresses and strains determined in CTC tests on the confining pressure p : **a** maximum ultimate strength and absolute dilatancy threshold (open points with crosses represent the deviated values); **b** axial and volumetric strain at failure and maximum volumetric strain

$$\epsilon_a^{(1D)} = \epsilon_c^{(2D)} - \epsilon_a^{(2D)}/2, \quad \epsilon_c^{(1D)} = \epsilon_a^{(2D)}/2, \quad (1)$$

where (1D) or (2D) state additional uniaxial or equibiaxial loading, respectively. It should be noted that any violation of the superposition principle for strains or violation of material isotropy can lead to formal tangential stiffness moduli that have different values for different loading paths.

4 Results and Discussion of Experiments with Monotonic Triaxial Loading

4.1 Results of Standard CTC Test Including Sample Failure

The experimental stress–strain characteristics of complete CTC tests for a set of initial isotropic pressures $p^{(i)}$ (from 10 to 120 MPa in increments of 10 MPa) are presented in

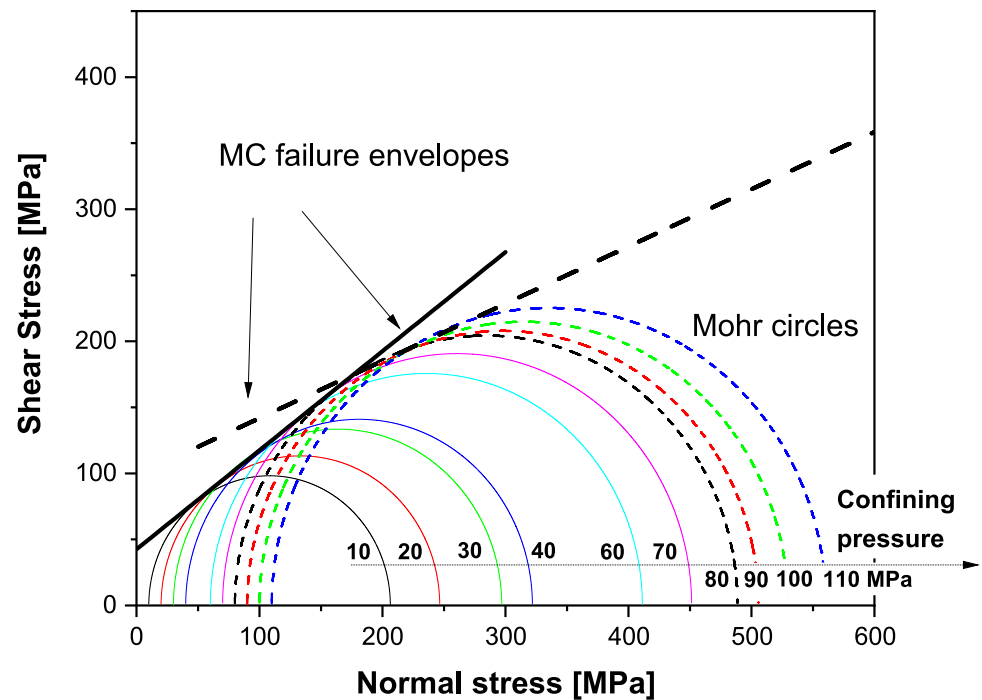
Fig. 5. The evaluated absolute dilatancy thresholds $\sigma_{D,TD}$,⁸ together with the maximum ultimate strengths $\sigma_{D,max}$, are summarized in Table 2. These two parameters increase almost monotonically with increasing initial isotropic pressure (Fig. 6). Some exceptions were only observed (see comments in Table 2), which can be attributed to a variability of rock sample properties. Moreover, the volumetric strain curve of sample 6 (60 MPa) in Fig. 5 shows a deviation at higher differential stress. This deviation mainly originates from the axial component of strain. This behavior is most likely to be due to the inhomogeneity of the sample in terms of local weakening of the material. The observed deviations coincide with differences in fracture modes deduced from the post-failure state of the sample. While the standard failure in full CTC tests was of the shear type, irregular fracture patterns were typically observed in samples showing anomalies in the deformation response. A characteristic feature of this fracture type was the initial horizontal orientation of the crack starting from the sample surface. Thus, these cracks follow latent fracture-surfaces that are formed by the layered structure of sedimentary rock.

The ultimate strength $\sigma_{D,max}$ increased gradually from about 200–450 MPa with increasing pressure $p^{(i)}$. These results are compatible with data from uniaxial tests on the same rocks in (Kwaśniewski and Rodríguez-Oitabén 2011). For the uniaxial test, the ratio $\sigma_{D,TD}/\sigma_{D,max}$ is about 0.5. With a raise of $p^{(i)}$ in our CTC tests, this ratio clearly increases to a value close to 1. Functional dependence $\sigma_{D,max}(p_i)$ almost exactly (except 120 MPa) follows the behavior of $\sigma_{D,TD}(p^{(i)})$ with an offset of about 50 MPa.⁹ Therefore, for pressures up to 110 MPa, detection of absolute dilatancy can be used as a reliable precursor of rock failure. Moreover, the function $\epsilon_{V,max}(p^{(i)})$ is monotonic without a visible deviation in comparison with the fluctuating values of $\epsilon_V(\sigma_{D,max}(p^{(i)}))$. Hence, the $\epsilon_{V,max}(p^{(i)})$ is a more representative parameter to describe rock deformational behavior. Analysis of the data in Fig. 6 showed that $\epsilon_{V,max}(p^{(i)})$ can be approximated using a linear function, while the difference $(\sigma_{D,max} - \sigma_{D,TD})$ was an almost constant parameter, which can be represented by the mean value of this difference. Thus, a combined strain–stress failure criterion could be considered for the investigated material. If the critical volumetric strain $\epsilon_{V,max}(p^{(i)}) = (0.0042 + 0.0000382\text{MPa}^{-1} \cdot p^{(i)}\{\text{MPa}\})$ is reached, then rock failure can start after increasing the differential stress σ_D by roughly 50 MPa.

⁸ The $\sigma_{D,TD} \equiv \sigma_D(\epsilon_{V,max})$, where the $\epsilon_{V,max}$ is the maximal volumetric strain.

⁹ For these reasons, the increase in the ratio $\sigma_{D,TD}/\sigma_{D,max}$ is only a consequence of the increased dilatancy threshold $\sigma_{D,TD}(p^{(i)})$.

Fig. 7 Mohr–Coulomb envelopes determined for Brenna sandstone from CTC tests at low and high pressures



The Mohr–Coulomb failure envelope was evaluated using the dependence of the ultimate differential stress on the initial confining pressure $p^{(i)}$ after removing two anomalous strengths for 50 and 120 MPa and demonstrates a bilinear dependency (Fig. 7). For $p^{(i)}$ up to 80 MPa, the angle of internal friction is about 37° with cohesion 43 MPa. For $p^{(i)}$ higher than 80 MPa, the angle decreased to approximately 23° , while the corresponding cohesion increased up to 99 MPa.

The anomalous (lower) strength was observed in the two tests in which the above-mentioned absolute dilatation threshold anomalies were found.¹⁰ These anomalies may be due to local defects, which develop into horizontal fractures during loading. The fractures terminate near the lateral surface of the sample, where a part of the material was released. Although sandstone appears very compact, latent defects cannot be completely ruled out.

4.2 Comparison of Experimental Data on Deformation in Quasi-Elastic Region Along Different Alternative Loading Paths

The stress–strain characteristics obtained from the tests are shown in Fig. 8 in the form of functional dependence of

stress difference σ_d on axial or circumferential strain. Figure 8a shows the original axial and lateral strains measured for the CTC–RTE tests (additional uniaxial loading–unloading) as a function of $\sigma_d = \Delta\sigma_v$. In Fig. 8b, the original experimental characteristics for the CTE–RTC tests (equibiaxial additional stress is applied) have been recalculated (through superposition principle and under the assumption of material isotropy) to formal strain response, which is equivalent to the uniaxial additional stress, and the sign of $\sigma_d = -\Delta\sigma_h = -\Delta p$ has been changed for a better comparison with the results of CTC–RTE.

A comparison of CTC and CTE loading paths revealed observable differences in the strain behaviors. The first observation is that the CTC axial strain curves corresponding to lower confining pressures show visible initial compaction of the material by increasing the differential stress σ_D . Meanwhile, in the CTE tests, almost no initial compaction part of the stress–strain characteristic can be observed. It should be noted that CTE characteristics for the two lowest pressures (10 MPa and 20 MPa) are missing because the feedback control of stress did not work properly at these pressures. Nevertheless, the differences in deformation behavior for pressures 30 MPa and higher are clearly visible. Meanwhile, increasing the initial isotropic pressure above 100 MPa causes substantial compaction of the sandstone and leads to a significant reduction in the observed differences for the CTC and CTE paths. For these high pressures, the dispersion of stress–strain curves is small, and the curves that are related to the axial strains are almost linear.

¹⁰ Since such deviations are common for rocks and the remaining measurements showed a monotonous trend, we did not repeat these deviated measurements, considering the limited number of samples that we wanted to keep for another study.

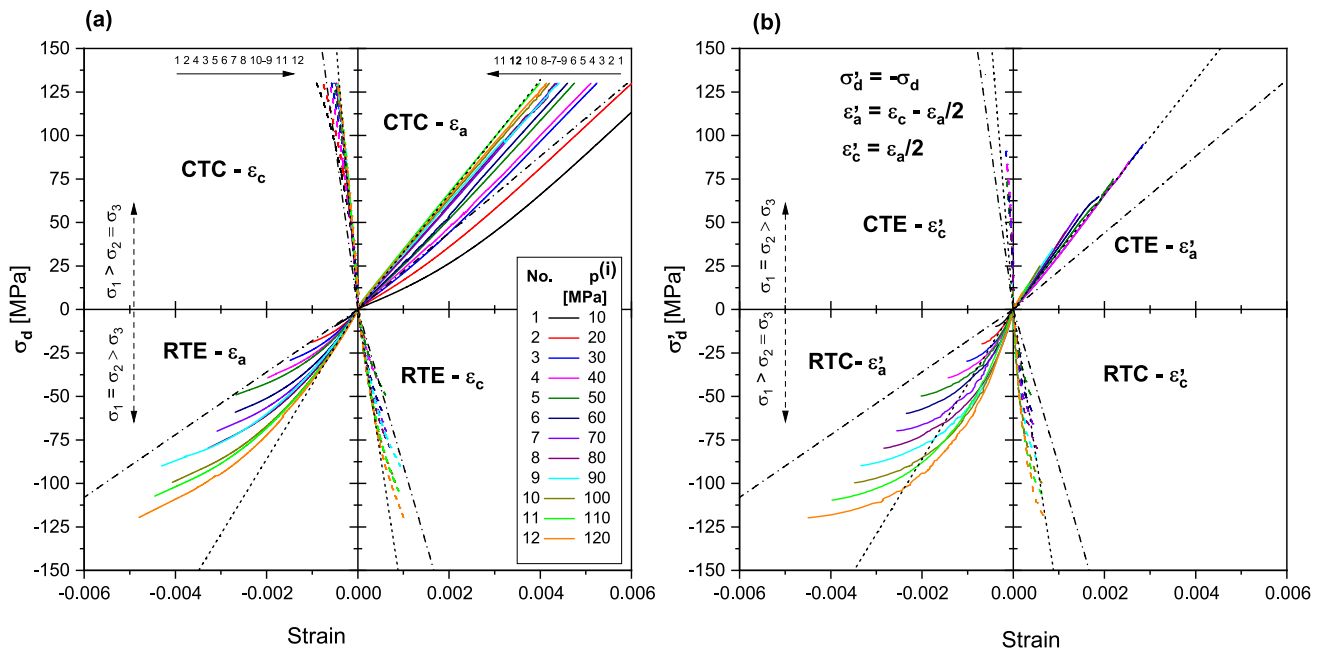


Fig. 8 Measured parts of stress–strain characteristics along: **a** CTC–RTE paths, and **b** CTE–RTC paths (recalculated to uniaxial response for better comparison). The dashed and dotted straight border lines delimit the groups of all RTE curves and CTC curves for $p^{(i)} \geq 30$

In particular, the nonlinear compaction parts of CTC curves for the axial strains are substantially suppressed.

In general, the recalculated formal CTE axial strains $\epsilon'_a = \epsilon_a^{(1D)}$ have lower values than the original axial strains ϵ_a for the CTC path at the same differential stress and confining pressure. Thus, the effective Young’s moduli estimated from slopes of linear parts of stress–strain curves for both paths differ (the rock is more stiff in the transverse than in the axial direction), which indicates a slight anisotropy of the material. In addition, for the CTE experiments, the formal transversal strains $\epsilon'_c = \epsilon_c^{(1D)}$ are very small. Their values are visibly less than the values of the lateral strains ϵ_c for the CTC experiments.

In particular, the higher initial compaction in the axial direction observed for CTC paths can be attributed to the compression of thin weak layers (and adjacent voids) oriented horizontally in the rock sample. The layers generated during the diagenetic process are sometimes indicated through lamination of rock material, but sometimes they are rather latent. However, they can be associated with the coalesced slit-like pores of approximately horizontal orientation of void space. The weak layers form natural fracture surfaces (Fig. 2). These layers in a rock sample can be efficiently compressed by a vertical load. Therefore, their role at high isotropic pressures is suppressed and the deformation response of rock material will be close to isotropic at these stress conditions. The small residual anisotropy observed at

MPa in graph **a**), and the same curves are plotted in graph **b**) for comparison. Due to technical problems in CTE tests at low pressures, the curves for 10 MPa and 20 MPa are not included

these high pressures can also be attributed to the preferred grain orientation in the sedimentary rock. The unloading characteristics that were measured in the RTE and RTC tests were extremely nonlinear from the beginning. However, the deformational characteristics of additional biaxial unloading (RTC) generally demonstrate a stiffer response than that of the uniaxial unloading (RTE) from the initial isotropic compression. Thus, the observed trend is the same as for loading paths.

4.3 Behavior of Effective Stiffness Moduli

The stiffness of the investigated material for all applied stress paths was evaluated through tangential moduli calculated from the stress–strain curves. Representative estimates of stiffness moduli are summarized for all of the tested samples in Tables 3 and 4. While all the tangential Young’s moduli dependences $E(\sigma_d)$ that are determined under the CTC and CTE conditions are approximately constant in the investigated stress region (with the exception of the stress region corresponding to the initial compaction), the Poisson’s ratio dependences $\nu(\sigma_d)$ can be approximated by increasing linear function. Therefore, only Poisson’s ratio limit values corresponding to the stress range of approximately constant Young’s modulus are presented in Table 3. The tangential Young’s moduli E for reduced paths are not constant due to the high non-linearity of the

Table 3 Representative stiffness moduli from conventional triaxial paths: E_1 —loading Young’s modulus (value in the stress region of approximate linearity of the axial strain), ν_1 —loading Poisson’s ratio (range of monotonic increase in the corresponding stress region)

Test (MPa)	E_1 (GPa)	ν_1 (range)	Test (MPa)	E_1 (GPa)	ν_1 (range)
CTC-10	24.0 ± 0.5	0.20–0.27	CTE-10	–	–
CTC-20	24.4 ± 0.2	0.17–0.23	CTE-20	–	–
CTC-30	27.0 ± 0.3	0.14–0.17	CTE-30	34.7 ± 0.4	0.05–0.10
CTC-40	27.3 ± 0.3	0.16–0.17	CTE-40	35.3 ± 0.8	0.05–0.10
CTC-50	28.6 ± 0.3	0.13–0.15	CTE-50	34.3 ± 1.1	0.07–0.08
CTC-60	30.5 ± 0.3	0.11–0.12	CTE-60	36.4 ± 0.6	0.03–0.09
CTC-70	30.1 ± 0.3	0.11–0.14	CTE-70	38.9 ± 0.7	0.01–0.08
CTC-80	30.5 ± 0.8	0.11–0.12	CTE-80	38.5 ± 0.7	0.01–0.07
CTC-90	30.4 ± 1.1	0.10–0.11	CTE-90	40.6 ± 0.7	0.01–0.06
CTC-100	30.8 ± 0.6	0.09–0.11	CTE-100	42.5 ± 0.4	0.01–0.04
CTC-110	32.3 ± 0.5	0.09–0.11	CTE-110	43.2 ± 0.9	0.03–0.08
CTC-120	31.4 ± 0.6	0.09–0.11	CTE-120	46.9 ± 1.1	0.01–0.02

experimental stress–strain curves. However, the dependence of these moduli on σ_d was approximately linear. Therefore, the intersections of corresponding linear fits with axis $\sigma_d = 0$ are presented in Table 4 as approximations of initial unloading Young’s moduli (i.e., estimate of intrinsic elastic moduli which are substantially higher than the effective loading moduli). The loading Young’s moduli in Table 3 are typically lower for CTC paths (additional axial compression) than for CTE paths (additional lateral compression). The reasons for this behavior (layered structure and preferable orientation of grains) were discussed in the preceding section. A similar trend can be observed for the unloading Young’s moduli in Table 4 (Fig. 9 illustrates the determination procedure for the moduli). The Young’s moduli for the RTE paths (axial unloading) are smaller than in the case of the RTC paths (lateral unloading). The observation may be a consequence of the preferred orientation of grains mentioned earlier. The rock material frame consisting of mineral grains should be stiffer in this preferred horizontal direction. A typical value of the unloading Poisson’s ratio is around 0.20 (with the exception of the two lowest isotropic pressures). CTC Poisson’s ratio decreases with increasing isotropic pressure, but increases

with increasing differential stress. Presented values of the Poisson’s ratio range from 0.09 to 0.27. The determined effective values of the CTE Poisson’s ratio are visibly lower (from 0.01 to 0.10) than the CTC values. While the Young’s modulus is mainly affected by the stiffness of mineral grains and their joints, the Poisson’s ratio is highly sensitive to the particular structure of materials. Therefore, an explanation of Poisson’s ratio behavior requires a detailed analysis of the layered structure and its role in strain measurements under triaxial loading and will be the subject of our other research.

A recent study Panaghi et al. (2021) focused on the effects of the stress path on the brittle failure of sandstone. In addition, a comparison of the constant Young’s moduli and Poisson’s ratio obtained using four different paths was given. However, the procedure for determining the Young’s modulus (or Poisson’s ratio) from the stress–strain curves of biaxial differential loading was not described by the authors of this study (Poisson’s effect was probably not considered). The magnitudes of the presented Young’s moduli changed with the stress path, while for Poisson’s ratio no pronounced systematic trend is observed. A comparison of the Young’s moduli for conventional paths (CTC and CTE) and reduced paths (RTC and RTE) shows in general higher values for the reduced variant. For comparison with our measurements, it should be taken into account that the values are not always presented for the equivalent confining pressures. However, even for equivalent confining pressures, the modulus for the RTC path was higher than for the CTC path, and the modulus for the RTE path was higher than for the CTE path. Thus, this trend is the same as in our measurements. For the conventional paths, these moduli were higher for compression than for extension, while a rather opposite trend was observed for the reduced paths. This behavior, therefore, does not completely match our observations. The authors, however, did not address the dependence of stiffness moduli on the path in detail. They promised to do so in a future study.

In the final discussion, it is necessary to evaluate the appropriateness of the approach using quasi-elastic coefficients for description of sedimentary material deformation in general triaxial conditions far enough from the state of failure. For example, in the case of granitic rocks, such a description usually works well. This may not apply to sedimentary rocks, as confirmed by the measurements made. The differences in the determined stiffness moduli that were observed during additional loading (conventional triaxial paths) and unloading (reduced triaxial paths) from an isotropic compression state can certainly be attributed, in particular, to the existence of irreversible processes during loading. The study of their role requires cyclic triaxial tests, the analysis of which is beyond the scope of this article of limited text length. However, it is possible to consider the application of linear theory at least for exclusively loading

paths, where constant coefficients will play the role of effective parameters. Due to the layered structure, it can be assumed that the sandstone meets approximate transverse isotropy. However, even in such a case, the data cannot be accurately described purely on the basis of the linear quasi-elastic description. The problem is the description of the transversal deformational response, which is not linear, and, moreover, the relationship $\epsilon_c = \epsilon'_c$ (given by the symmetry of the stiffness matrix) is not well satisfied for measured data. Therefore, a nonlinear phenomenological description should be used for a more accurate description of sandstone deformation in general triaxial conditions. However, for a rough description of the deformation for geotechnical applications, the determined stiffness moduli (which are a function of the initial isotropic pressure) can still be useful, especially if the variability of the mechanical properties of the natural material is taken into account.

5 Conclusions

An experimental study of Brenna sandstone deformation in several representative triaxial loading modes, together with a detailed analysis of rock composition and structure, was performed. The main subject of the planned triaxial experiments was an investigation of the deformation of the Brenna sandstone in the so-called quasi-elastic region under four alternative regimes of loading CTC, RTE, CTE, and RTC. The initial study was focused on loading experiments with a monotonic change of differential stress. For the CTC path, complete stress–strain characteristics were also measured which evince considerable volumetric dilatancy of the sandstone. The threshold of the absolute volumetric dilatancy, as well as the ultimate strength, increased with increasing isotropic pressure p . Rock failure occurs after an approximately constant stress increment that follows the onset of dilatancy (a pre-failure indicator). Hence, for CTC paths,

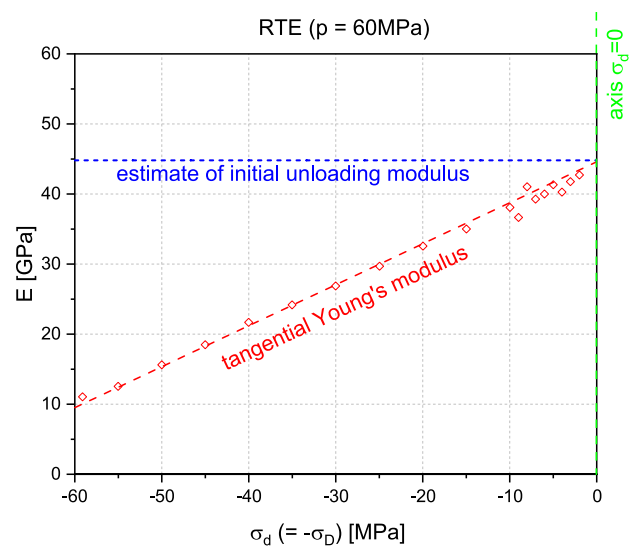


Fig. 9 Determination of an estimate of the initial unloading Young’s modulus E_u for reduced paths. Example of the intersection of the extrapolated tangential modulus curve $E(\sigma_d)$ with the vertical axis ($\sigma_d = 0$)

this failure can be determined through the approximate combined stress–strain criterion.

The deformational behavior of the sandstone well below the ultimate strength was analyzed with respect to different loading/unloading paths. For given isotropic pressure and differential stress, the longitudinal deformation (i.e., deformation in the applied stress direction) under axial loading is higher than for lateral loading. At low isotropic pressures, initial compaction of the sedimentary material in the axial direction (perpendicular to the stratification) can even be observed under axial loading in the CTC test. This anisotropic behavior can be explained by the existence of a layered structure (weak layers forming natural fracture surfaces that are approximately perpendicular to the axial direction). Similar differences in rock deformation were observed for axial and lateral unloading (reduced triaxial paths). The

Table 4 Representative stiffness moduli from reduced triaxial paths: E_u —initial unloading Young’s modulus (estimate corresponding to the intersection of the linear fit of the tangential Young’s modulus curve with the line $\sigma_d = 0$), and ν_u —unloading modulus (constant fit of approximately constant tangential Poisson’s ratio

Test (MPa)	E_u (GPa)	ν_u	Test (MPa)	E_u (GPa)	ν_u
RTE-10	28.7 ± 0.9	0.16 ± 0.03	RTC-10	39.9 ± 10.6	0.12 ± 0.02
RTE-20	38.1 ± 2.2	0.17 ± 0.02	RTC-20	60.0 ± 2.6	0.15 ± 0.01
RTE-30	38.2 ± 0.2	0.19 ± 0.01	RTC-30	74.5 ± 2.6	0.21 ± 0.01
RTE-40	39.6 ± 0.4	0.21 ± 0.01	RTC-40	78.1 ± 2.3	0.19 ± 0.01
RTE-50	39.7 ± 0.5	0.24 ± 0.01	RTC-50	70.6 ± 4.3	0.23 ± 0.01
RTE-60	44.8 ± 0.2	0.20 ± 0.01	RTC-60	79.6 ± 1.9	0.20 ± 0.01
RTE-70	46.2 ± 0.2	0.21 ± 0.01	RTC-70	81.6 ± 3.4	0.22 ± 0.01
RTE-80	46.8 ± 0.2	0.22 ± 0.01	RTC-80	98.7 ± 1.9	0.20 ± 0.01
RTE-90	43.8 ± 0.2	0.22 ± 0.01	RTC-90	97.2 ± 1.9	0.19 ± 0.01
RTE-100	48.1 ± 0.3	0.20 ± 0.01	RTC-100	94.2 ± 1.3	0.18 ± 0.01
RTE-110	47.8 ± 0.3	0.21 ± 0.01	RTC-110	79.6 ± 1.0	0.17 ± 0.01
RTE-120	49.0 ± 1.1	0.20 ± 0.01	RTC-120	97.6 ± 3.9	0.18 ± 0.02

values and behavior of the determined effective stiffness moduli corresponding to the different stress paths differ as a consequence of observed differences in rock deformation that reflects the rock anisotropy (which is of diagenetic origin). Moreover, only the loading Young's moduli are almost constant, while loading Poisson's ratios linearly increase with increasing differential stress (Fig. 9).

In addition, to understand the deformation behavior during reduced triaxial stress paths, it is convenient to analyze the role of irreversible processes. The triaxial experiment can be augmented by cyclic variants of triaxial stress tests to evaluate the inelastic deformation of the sandstone. This topic is the focus of our further study.

Appendix 1: Servo-Controlled Rock Mechanics System: Parameters

The multipurpose experimental rock mechanics system is designed not only for the standard uniaxial tests (i.e., the compressive test, tensile test, indirect tension test, and fracture toughness test). Schemes and photos of this device and the setup of a sample for triaxial tests are shown in Fig. 10 Using the triaxial chamber (MTS 656.06), this equipment also allows to perform special triaxial experiments. The maximal pressure in the chamber can reach magnitudes up to 140 MPa. In addition, pore pressures up to the same maximum value of 140 MPa can be applied to the measured sample. The temperature of a rock sample can be controlled from the room temperature to 200 °C. Load frame (MTS 315.04) is designed for 4.6 MN in compression and 2.3 MN in tension; its stiffness is 10.5 GN/m. The whole measuring system is controlled by a computer through the supplied software. Reliable control of the experiment asks for tuning the feedback of the system with the installed sample and the implementation of measuring methodology in the form of software procedures. A triaxial chamber with a high inner volume enables installation of a dynamometer (in our measurements MTS 661.98 with 2600 kN limit), and samples of maximal diameter 100 mm and height 250 mm with a pair of attached high precision extensometers (dual axial, and circumferential chain extensometer). In the presented measurements, a diameter and gauge length equal to 50 mm were used. Signals from two independent channels of the axial extensometer are averaged to get the value of pure axial strain ϵ_a . The confining fluid pressure is generated by a confining pressure intensifier MTS 286.20 and is measured through a pressure gauge near the intensifier piston. The present experiments were performed under undrained, and unsaturated conditions. However, if needed, the desired fluid pressure in the pores can be generated through the analogous intensifier MTS 286.30. The alternative tests (CTE, RTE, and RTC)

must be realized with hermetically sealed pressing ends. Standard ends can only be used for standard CTC tests. However, comparative CTC tests performed did not show a difference in the results obtained using sealed or standard ends.

Appendix 2: Mechanical Characteristics of an Idealized Material and Non-standard Loading Paths

The deformation of an elastic isotropic homogeneous sample of cylindrical shape (with symmetry axes oriented vertically) in an axisymmetric triaxial state can be described by the following set of equations:

$$\epsilon_a = \frac{\sigma_v}{E} - 2\frac{\nu}{E}\sigma_h \quad \text{and} \quad \epsilon_c = \frac{\sigma_h}{E} - \frac{\nu}{E}(\sigma_h + \sigma_v), \quad (2)$$

where ϵ_a and ϵ_c are axial and circumferential strains representing the sample deformation starting from reference unloaded state:

$$\epsilon_a \equiv -(l - l_0)/l_0 \quad \epsilon_c \equiv -(d - d_0)/d_0,$$

where the reversal sign convention (being standard in geomechanics) is used (i.e., compressive/extension stresses and strains are considered to be positive/negative). The $\sigma_h = p$ and $\sigma_v = \sigma_d + p$ represent horizontal and vertical stress components, whose values differ by σ_d . The parameters E and ν in Eq. (2) are the Young's modulus and Poisson's ratio.

The stress applied to the sample follows one of the four loading paths (CTC, RTE, CTE, or RTC), as shown in Fig. 4. Each of these paths consists of two phases: initial isotropic loading to the starting point i of the second phase and differential loading/unloading to the end point f . The total deformation represents the sum of two members:

$$\epsilon_a = \epsilon_a^{(i)} + \Delta\epsilon_a^{(f)},$$

$$\epsilon_c = \epsilon_c^{(i)} + \Delta\epsilon_c^{(f)}.$$

The first member originates from the isotropic compression, and the second member is related to the following differential loading/unloading. For the isotropic loading to the pressure $p^{(i)}$ (i.e., $\sigma_v^{(i)} = p^{(i)}$, and $\sigma_h^{(i)} = p^{(i)}$), Eq. (2) gives

$$\epsilon_a^{(i)} = \frac{1 - 2\nu}{E}p^{(i)} \quad \text{and} \quad \epsilon_c^{(i)} = \frac{1 - 2\nu}{E}p^{(i)},$$

and volumetric strain dependence on acting isotropic pressure can be expressed as

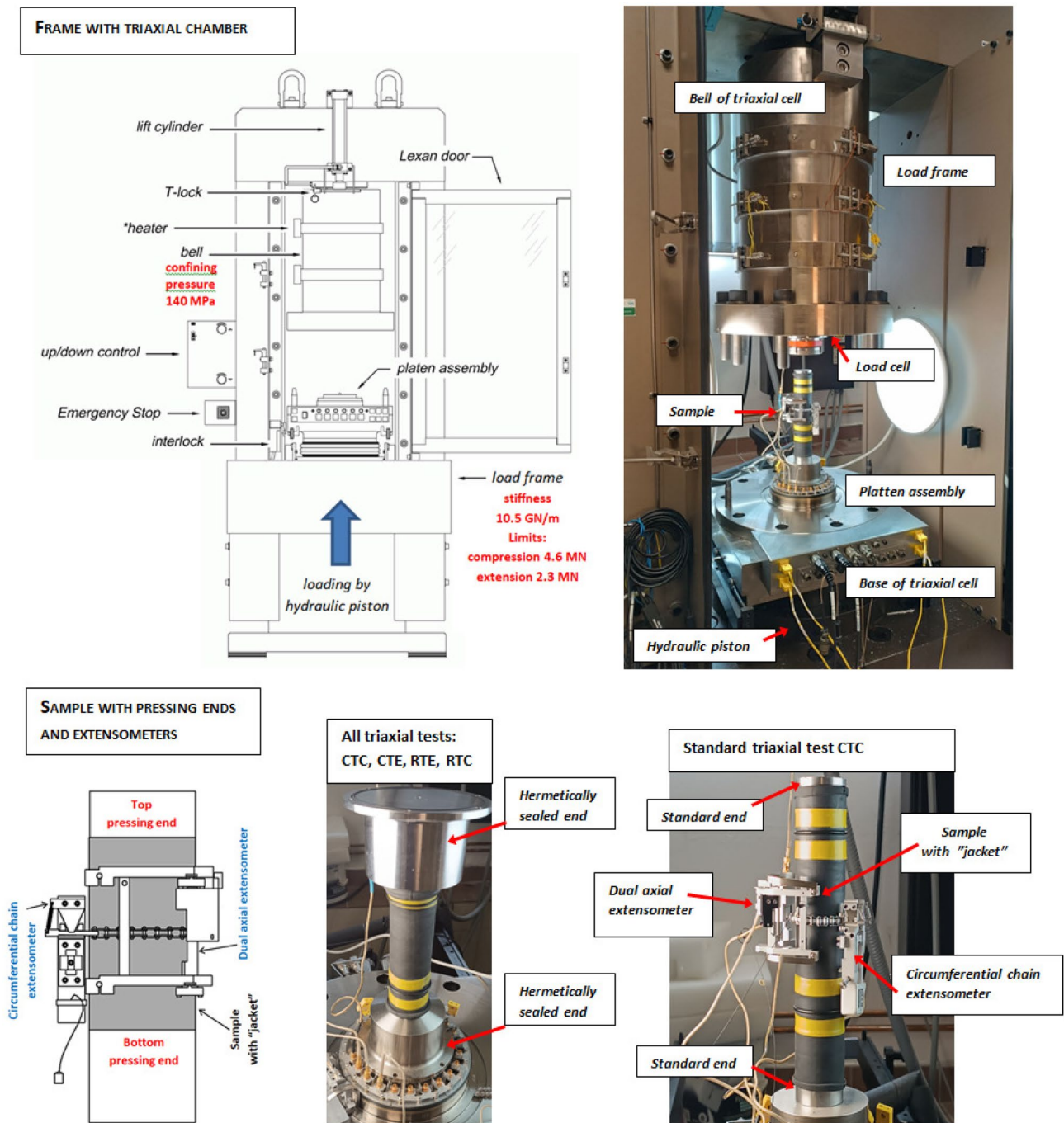


Fig. 10 Experimental device and installed sample with pressing ends and extensometers (schemes are based on drawings from manuals of MTS Systems Corporation)

$$\epsilon_v^{(i)} = \epsilon_a^{(i)} + 2\epsilon_c^{(i)} = K^{-1}p^{(i)}, \text{ where } K \equiv \frac{E}{3(1-2\nu)}, \quad (3)$$

which is very well known as the bulk modulus (of compressibility). After the initial loading to the point i , the second part of the total path through stress space to a point f is realized.

For paths CTC and RTE, the confining fluid pressure is constant $p = p^{(i)}$, and the vertical stress is gradually changed to the desired final value $\sigma_v = p^{(i)} + \Delta\sigma_v^{(CTC/RTE)}$ ($\Delta\sigma_v^{(CTC)} > 0$ and $\Delta\epsilon_a^{(CTC)} > 0$, i.e., axial compression, or $\Delta\sigma_v^{(RTE)} < 0$ and $\Delta\epsilon_a^{(RTE)} < 0$, i.e., axial extension). Equation (2) are transformed on

$$\begin{aligned} \epsilon_a &= \epsilon_a^{(i)} + \frac{1}{E} \Delta\sigma_v^{(CTC/RTE)} \quad \text{and} \\ \epsilon_c &= \epsilon_c^{(i)} - \frac{\nu}{E} \Delta\sigma_v^{(CTC/RTE)}. \end{aligned}$$

By differentiation axial and circumferential strains with respect to variable $\Delta\sigma_v$, we get

$$\left. \frac{\partial \epsilon_a}{\partial \Delta\sigma_v} \right|_{\Delta p=0} = \frac{1}{E} \quad \text{and} \quad \left. \frac{\partial \epsilon_c}{\partial \Delta\sigma_v} \right|_{\Delta p=0} = -\frac{\nu}{E},$$

Then, after simple mathematical calculations, we obtain the formulae for the calculations of the stiffness modules from the CTC and RTE tests in the traditional form that is used to interpret the uniaxial tests:

$$E_{(CTC/RTE)} = \left. \frac{\partial \Delta\sigma_v}{\partial \epsilon_a} \right|_{\substack{\epsilon_a > \epsilon_a^{(i)} \\ \epsilon_a < \epsilon_a^{(i)}, \Delta p=0}} = \left. \frac{\partial \sigma_d}{\partial \epsilon_a} \right|_{p=p^{(i)}} \quad (4)$$

$$\nu_{(CTC/RTE)} = - \left. \frac{\partial \epsilon_c}{\partial \epsilon_a} \right|_{\substack{\epsilon_a > \epsilon_a^{(i)} \\ \epsilon_a < \epsilon_a^{(i)}, \Delta p=0}}. \quad (5)$$

In the case of CTE, and RTC paths, the confining fluid pressure varies monotonically, and its instantaneous value is $p = p^{(i)} + \Delta p$, while the vertical stress is kept to be constant $\sigma_v = p^{(i)}$ ($\Delta p^{(CTE)} > 0$ and $\Delta\epsilon_a^{(CTE)} < 0$, i.e., axial extension, or $\Delta p^{(RTC)} < 0$ and $\Delta\epsilon_a^{(RTC)} > 0$, i.e., axial compression). The expressions in Eq. (2) can be converted to the form

$$\begin{aligned} \epsilon_a &= \epsilon_a^{(i)} - \frac{2\nu}{E} \Delta\sigma_h^{(RTC/CTE)} \quad \text{and} \\ \epsilon_c &= \epsilon_c^{(i)} + \frac{1-\nu}{E} \Delta\sigma_h^{(RTC/CTE)}. \end{aligned}$$

Differentiation of axial and circumferential strains with respect to variable $\Delta\sigma_h \equiv \Delta p$ leads to the relation

$$\left. \frac{\partial \epsilon_a}{\partial \Delta p} \right|_{\Delta\sigma_v=0} = -\frac{2\nu}{E} \quad \text{and} \quad \left. \frac{\partial \epsilon_c}{\partial \Delta p} \right|_{\Delta\sigma_v=0} = \frac{1-\nu}{E}.$$

After some simple calculations, we obtain the formulae for the determination of stiffness modules from CTE and RTC tests.

$$E_{(CTE/RTC)} = -2\nu_{(CTE/RTC)} \left. \frac{\partial \Delta p}{\partial \epsilon_a} \right|_{\substack{\epsilon_a < \epsilon_a^{(i)} \\ \epsilon_a > \epsilon_a^{(i)}, \Delta\sigma_v=0}} = 2\nu_{(CTE/RTC)} \left. \frac{\partial \sigma_d}{\partial \epsilon_a} \right|_{\sigma_v=p^{(i)}} \quad (6)$$

$$\nu_{(CTE/RTC)} = 1 / \left(1 - 2 \left. \frac{\partial \epsilon_c}{\partial \epsilon_a} \right|_{\substack{\epsilon_a > \epsilon_a^{(i)} \\ \epsilon_a < \epsilon_a^{(i)}, \Delta\sigma_v=0}} \right). \quad (7)$$

These formulae differ from the traditional ones that are commonly used for uniaxial, or for CTC and RTE tests. This fact should be taken into account in a comparison of the stress–strain characteristics obtained from CTC–RTE and CTE–RTC tests. For example, for CTE, the Young’s modulus cannot be directly estimated from the slope of the original stress–strain curves, as is the case of CTC or uniaxial compression.

Acknowledgements This work was supported by the following projects: Grant no CZ.1.05/2.1.00/ 03.0082—“Institute of Clean Technologies for Mining and Utilization of Raw Materials for Energy Use” of the “Research and Development for Innovations Operational Programme,” co-financed by Structural Funds of the European Union; project LO1406—“Institute of Clean Technologies for Mining and Utilization of Raw Materials for Energy Use—Sustainability Program” of the National Programme of Sustainability (NPU I) funded by the Ministry of Education, Youth and Sports of the Czech Republic; project LM2015084—“RINGEN-Research Infrastructure for Geothermal Energy” of “Program Large Infrastructures for Research” funded by the Ministry of Education, Youth and Sports of the Czech Republic; Grant no CZ.02.1.01/0.0/0.0/16_013/0001792—“RINGEN-Research Infrastructure Upgrade” of “Operational Programme Research, Development and Education”; and a grant from the Czech Science Foundation (18-25035S).

Funding Open access publishing supported by the National Technical Library in Prague.

Data availability All treated data is provided as figures and tables in the manuscript. Some available raw data can be obtained upon request.

Declarations

Conflict of interest The authors declare that they have no conflict of interest. There was no financial or personal relationships with other people or organizations that can inappropriately influence our work. There is no professional or other personal interest that could be construed as influencing the review of this manuscript.

Open Access This article is licensed under a Creative Commons Attribution 4.0 International License, which permits use, sharing, adaptation, distribution and reproduction in any medium or format, as long as you give appropriate credit to the original author(s) and the source, provide a link to the Creative Commons licence, and indicate if changes were made. The images or other third party material in this article are included in the article’s Creative Commons licence, unless indicated otherwise in a credit line to the material. If material is not included in the article’s Creative Commons licence and your intended use is not permitted by statutory regulation or exceeds the permitted use, you will

need to obtain permission directly from the copyright holder. To view a copy of this licence, visit <http://creativecommons.org/licenses/by/4.0/>.

References

- Ayatollahi MR, Nejati M, Ghoulis S (2022) Crack tip fields in anisotropic planes: a review. *Int J Fract* 234(1–2):113–139
- Böker R (1914) Versuche, die Grenzkurve der Umschlingungsversuche und der Druckversuche zur Deckung zu bringen. Ph.D. thesis, Dissertation, Königliche Technische Hochschule zu Aachen
- Böker R (1915) Die Mechanik der bleibenden Formänderung in kristallinisch aufgebauten Körpern. *Ver Dtsch Ing Mitt Forsch* 175:1–51
- Cen D, Huang D (2017) Direct shear tests of sandstone under constant normal tensile stress condition using a simple auxiliary device. *Rock Mech Rock Eng* 50(6):1425–1438
- Feng X-T, Haimson B, Li X, Chang C, Ma X, Zhang X, Ingraham M, Suzuki K (2019) ISRM suggested method: determining deformation and failure characteristics of rocks subjected to true triaxial compression. *Rock Mech Rock Eng* 52(6):2011–2020
- Fjar E, Holt RM, Raaen A, Risnes R, Horsrud P (2008) *Petroleum related rock mechanics*, vol 53. Elsevier, New York
- Franklin J (1983) Suggested methods for determining the strength of rock materials in triaxial compression: revised version. *Int J Rock Mech Min Sci Geomech Abstr* 20(6):285–290
- Ingraham M, Issen K, Holcomb D (2012) Compactant features observed under true triaxial states of stress. In: 46th US rock mechanics/geomechanics symposium. OnePetro
- Ingraham M, Issen K, Holcomb D (2013a) Response of Castlegate sandstone to true triaxial states of stress. *J Geophys Res Solid Earth* 118(2):536–552
- Ingraham MD, Issen KA, Holcomb DJ (2013b) Use of acoustic emissions to investigate localization in high-porosity sandstone subjected to true triaxial stresses. *Acta Geotech* 8(6):645–663
- Kwaśniewski M (2012) Mechanical behavior of rocks under true triaxial compression conditions: a review. In book: *True triaxial testing of rocks*. Geomechanical Research Series, Vol.4. CRC Press/Balkema, Leiden, pp 99–138
- Kwaśniewski M, Rodríguez-Oitabén P (2011) Study on the dilatancy angle of rocks in the pre-failure domain. In: *Harmonising rock engineering and the environment (proceedings of the 12th international congress on rock mechanics)*. ISRM
- Kwaśniewski M, Takahashi M (2010) Strain-based failure criteria for rocks: state of the art and recent advances. In: *Rock mechanics in civil and environmental engineering*. CRC Press, pp 45–56
- Liu Z, Ma C, Wei X, Xie W (2021) Experimental study of rock subjected to triaxial extension. *Rock Mech Rock Eng* 55(5):21–29
- Ma X, Haimson BC (2016) Failure characteristics of two porous sandstones subjected to true triaxial stresses. *J Geophys Res Solid Earth* 121(9):6477–6498
- Murrell S (1963) A criterion for brittle fracture of rocks and concrete under triaxial stress and the effect of pore pressure on the criterion. *Proc., Fifth Rock Mech. Sympo.* (ed. by Fairhurst, C.), Pergamon, pp. 563–577
- Panaghi K, Takemura T, Asahina D, Takahashi M (2021) Effects of stress path on brittle failure of sandstone: difference in crack growth between tri-axial compression and extension conditions. *Tectonophysics* 810:228865
- Pantelev I, Mubassarova V, Zaitsev A, Karev V, Kovalenko YF, Ustinov K, Shevtsov N (2020a) The Kaiser effect under multiaxial nonproportional compression of sandstone. In: Garnov SV (ed) *Doklady physics*, vol 65. Springer, pp 396–399
- Pantelev I, Mubassarova V, Zaitsev A, Shevtsov N, Kovalenko YF, Karev V (2020b) Kaiser effect in sandstone in polyaxial compression with multistage rotation of an assigned stress ellipsoid. *J Min Sci* 56(3):370–377
- Ramsey J, Chester F (2004) Hybrid fracture and the transition from extension fracture to shear fracture. *Nature* 428(6978):63–66
- Takahashi N, Takahashi M, Park H, Fujii Y, Takemura T (2012) Deformation and strength characteristics of Kimachi sandstone under confined compression and extension test conditions. *True Triaxial Test Rocks* 4:235–242
- Takemura T, Suzuki K, Golshani A, Takahashi M (2012) Stress path dependency of failure mechanism from the viewpoint of dilatant behavior. In book: *True triaxial testing of rocks*. Geomechanical Research Series, Vol.4. CRC Press/Balkema, Leiden, pp 235–242
- Ulusay R, Hudson J et al (1974) The complete ISRM suggested methods for rock characterization. *Test Monit* 2006(2007):628
- von Kármán T (1911) Festigkeitsversuche unter allseitigem Druck. *Z Ver Dtsch Ing* 55:1749–1757
- Zeng B, Huang D, Ye S, Chen F, Zhu T, Tu Y (2019) Triaxial extension tests on sandstone using a simple auxiliary apparatus. *Int J Rock Mech Min Sci* 120:29–40
- Zhu W, Montesi LG, Wong T-F (1997) Shear-enhanced compaction and permeability reduction: triaxial extension tests on porous sandstone. *Mech Mater* 25(3):199–214

Publisher's Note Springer Nature remains neutral with regard to jurisdictional claims in published maps and institutional affiliations.